Isothermal Calorimetry Evaluation of Metallurgical Silicon as a Negative Electrode Material for Li-Ion Batteries

Journal of The Electrochemical Society, 2021 **168** 030504

Isothermal Calorimetry Evaluation of Metallurgical Silicon as a Negative Electrode Material for Li-Ion Batteries

V. L. Chevrier,[1,*,z] Zilai Yan,[2,] Stephen L. Glazier,[3] M. N. Obrovac,[2,4,*] and L. J. Krause[1,*]**

[1]*Cyclikal, Saint Paul, Minnesota, United States of America*
[2]*Department of Chemistry, Dalhousie University, Halifax, NS, Canada*
[3]*Novonix, Bedford, NS, Canada*
[4]*Department of Physics and Atmospheric Science, Dalhousie University, Halifax, NS, Canada*

The structural evolution of Si during lithiation and delithiation is uniquely dependent on the cycling conditions and can show either reversible or path dependent behavior. In this paper, metallurgical Si (large crystalline particles of pure Si) is cycled to exhibit both reversible and path dependent cycling while in-operando calorimetry is performed with a high precision isothermal calorimeter. The enthalpy potential and waste heat are studied in both the reversible and path dependent regimes. The enthalpy of crystallization of $Li_{15}Si_4$ is quantified to be 21 kJ mol_{Si}^{-1}. The parasitics (heat of side reactions) of pure Si are studied, showing a stronger current than time dependence. The voltage dependence of the parasitic power is quantified, showing increasing parasitics below 170 mV. The results of this in depth calorimetric study of metallurgical Si provides valuable insights into the heat production and energy efficiency of Si as a negative electrode material in Li-ion batteries.
 [DOI: 10.1149/1945-7111/abe16a]

Manuscript submitted December 7, 2020; revised manuscript received January 14, 2021. Published March 1, 2021.

Silicon has long been considered as a negative electrode material to increase the energy density of Li-ion batteries.[1] In 2003, the lithiation-induced amorphization of crystalline Si was demonstrated,[2] and in 2004 the crystalline $Li_{15}Si_4$ phase occurring at the end of amorphous Si lithiation was identified.[3] Subsequent in situ X-ray diffraction studies mapped out the path in phase space taken by lithiated Si depending on voltage cutoffs.[4] First principles DFT calculations and in situ Mössbauer measurements have elucidated the local Li-Si environments giving rise to the features of the Si voltage curve.[5–7]

The voltage curve of Si presents significant hysteresis. A component of the hysteresis is rate independent, indeed the hysteresis remains unchanged at currents as low as C/1000.[6] A number of explanations have been given for the hysteresis found in the Si voltage curve, yet a careful thermal analysis of Si cycling which includes a calorimetric characterization of $Li_{15}Si_4$ formation has never been published. In this paper, the enthalpy potential approach of Assat et al.[8] is used to characterize the heat production of Si and explicitly characterize the path dependence of heat production, the enthalpy of crystallization of $Li_{15}Si_4$ is quantified, and the parasitics (heat of side reactions) found in Si are discussed.

The present study builds on the use of isothermal microcalorimetry as a tool to study Li-ion batteries, which has been used to study positive[9–11] and negative[12–15] electrode materials in half cells, as well as in symmetrical[12,13] and full cells.[16–23] It is also complementary to the work of Li et al. and Housel et al. who studied the reactivity of nano Si electrodes using isothermal microcalorimetry.[14,15] These quantified the parasitics of nano Si in its initial cycles and quantified the entropy component of the heat flow by studying the variation of voltage with temperature.

Thermodynamic Considerations

The power measured by an isothermal calorimeter ($\dot{q}$) when cycling a cell can be expressed as

$$\dot{q} = I\eta + \frac{IT}{nF}\frac{dS}{dx} + \dot{q}_p \qquad [1]$$

where I is the current (negative for discharge, in the case of Si this would be lithiation), η the overpotential (negative for discharge, positive for charge), T the temperature, F Faraday's constant, n the number of electrons involved in the half-reaction per the stoichiometric Li content (x), S the entropy and $\dot{q}_p$ the parasitic power.[12] Considering the overpotential as $\eta = V - U$, where V is the measured voltage (cell potential) and U the equilibrium potential and assuming the parasitic power is sufficiently constant that it can be subtracted, one can express the enthalpy potential U_H as:[8]

$$V - \frac{\dot{q}|_{T,P}}{I} = U - \frac{T}{nF}\frac{dS}{dx} = U_H \qquad [2]$$

For a reversible process U_H should be identical on lithiation and delithiation. The difference between the equilibrium potential and the enthalpy potential can be seen as the entropy contribution

$$U - U_H = \frac{T}{nF}\frac{dS}{dx} \qquad [3]$$

Furthermore, for a reversible process, the equilibrium potential can be expressed as

$$U = V_+ - \frac{\dot{q}_+ - \dot{q}_-}{2I} = V_+ + \frac{\dot{q}_+ - \dot{q}_-}{2I} = \frac{V_+ - V_-}{2} \qquad [4]$$

Finally, the enthalpy potential is a convenient metric to consider in the context of heat production of cells since it is current independent and the heat production of a cell can be calculated as

$$\dot{q} = I(V - U_H) \qquad [5]$$

Therefore, the heat production under a broad range of cycling conditions can be estimated with the enthalpy potential, regardless of whether the process is reversible.

The above analysis neglects contributions from the heat of mixing. The heat of mixing can be generated by concentration gradients across the electrode due to non-uniform current distribution, across the electrolyte due to mass transfer, and within particles due to diffusion.[11,24,25] A recent study by Chalise et al. quantified the contribution from the heat of mixing as being significant above 1C rates. In this study, the electrodes are very thin and porous, and rates are C/5 or less. The enthalpy of mixing can therefore be ignored, and

*Electrochemical Society Member.
**Electrochemical Society Student Member.
[z]E-mail: vincent@cyclikal.com

as shown below, the current independence of the measured enthalpy potential supports this assumption.

Methods

Materials synthesis and coin cell assembly.—Si electrodes were composed of Si powder (99.999%, 325-mesh, SkySpring Nanomaterials, Inc.), carbon black (CB) (Super C65, Imerys Graphite and Carbon), and lithium polyacrylate (LiPAA) (from a 10 wt% LiPAA aqueous solution, made by neutralizing a polyacrylic acid solution (average molecular weight ~250,000 g mol^{-1}, 35 wt% in H_2O, Sigma-Aldrich) with $LiOH{\cdot}H_2O$ (≥98.0%, Sigma-Aldrich) in distilled water) in a volumetric ratio of 70/5/25. Distilled water/isopropyl alcohol (1:1 in volume) was added to this mixture to adjust viscosity. Slurry mixing was conducted for one hour using a planetary ball mill (Retsch PM200) with three 13 mm tungsten carbide balls at 100 rpm. Electrodes were cast from distilled water slurries onto copper foil with a 0.002-inch coating bar, then air dried at 120 °C for 1 h, cut into 1.3 cm disks (1.33 cm^2), then heated under vacuum for 1 h at 120 °C and assembled into cells with no further air exposure. The mass loading of coatings is 0.53–0.68 mg cm^{-2}. Due to the low mass loading, large errors in capacity measurements are expected.[26,27]

Coin cell construction was conducted in an Ar-filled glovebox using standard 2325 coin cell hardware. Electrolyte was prepared using 1 M $LiPF_6$ in an electrolyte solvent composed of 3:7 (by weight) ethylene carbonate (EC):ethyl methyl carbonate (EMC) and fluoroethylene carbonate (FEC) (9:1 by volume) (all battery grade from BASF). Two layers of Celgard-2300 separator and one layer of polyethylene blown microfiber separator (BMF) (3M Company) were used as cell separators. Each electrode was paired with a 2.57 cm^2 circular lithium metal (thickness of 0.38 mm, 99.9%, Sigma-Aldrich) electrode.

Scanning electron microscope (SEM) images were collected using a JEOL 840 SEM. X-ray diffraction (XRD) patterns were obtained using a Rigaku Ultima IV diffractometer equipped with a Cu Kα X-ray source, a diffracted beam graphite monochromator, and a scintillation detector. Particle size distribution (PSD) was measured using a Partica LA-950V2 laser scattering particle size distribution analyzer (Horiba, Japan). Specific surface area (SSA) was measured using a Micromeritics Flowsorb II 2300 surface area analyzer with the single-point Brunauer–Emmett–Teller (BET) method. Three sets of absorption and desorption data were used for each sample. For XRD, PSD, and SSA characterizations, Si coating samples were gently collected with a scalpel from thick Si electrodes (electrode slurries were cast with a 0.012-inch coating bar).

Electrochemical and calorimetry measurements.—Keithley 2602B source-measure units were used to charge and discharge the cells. Measurements were performed in the 1 mA and 0.1 mA ranges with accuracies of 400 nA and 45 nA respectively. Voltage measurements were performed in the 6 V range with an accuracy of 2 mV.

The heat flow calorimeter is a TAM III (Thermally Activated Module, TA Instruments) with 12 microcalorimeters. The temperature used throughout this work was 40 °C. The TAM III is capable of controlling the bath temperature to within a few micro-degrees centigrade. References 12, 21 describe the method and modifications made to the TAM III to allow in-operando calorimetry measurements on Li-ion coin cells. The general calibration procedure was described earlier for coin cells.[12] In this work the procedure was very similar with the exception that the precision resistor (200 Ohm, 0.1%) was placed on the outside of the crimped dry coin cell. Errors of 2 μW are estimated for the current setup. Considering the average of the cell weights used in the experiments, this corresponds to an error of approximately 2 mW g^{-1}.

In most cases the coulombic efficiency of the Si electrodes was poor. To calculate the lost electrical heat (hysteresis of the voltage capacity curve) the voltage capacity curves were scaled to have the same capacity, namely the average of charge and discharge. When gravimetric heats are stated (e.g. mWh g^{-1}) the mass is *not* the total electrode mass, but the mass estimated from the capacity with the assumption that full capacity of Si is 3578 mAh g^{-1} ($Li_{15}Si_4$). Finally, as in Assat et al.,[8] a constant term has been subtracted from the power to compensate for the parasitic term in Eq. 1, in this case 2.1 μW. This was estimated as the average parasitic heat flow, a more detailed study of the parasitics is found in the section "Parasitics of Reversible Si Cycling."

Results and Discussion

Electrodes and Si particles.—The Si electrodes in this study were designed to be an accurate representation of the behavior of metallurgical macroscopic crystalline Si in a Li-ion cell. The cell is therefore not designed for cycle life. Indeed Si−based materials for Li-ion batteries are typically highly engineered to address the challenges of pure macroscopic Si, primarily its large expansion and pulverization, and its electrolyte reactivity.[1] Engineered Si−based materials therefore have far superior cycling performance than pure macroscopic crystalline Si, however they introduce design-related behavior that make them poor candidates for a reference thermal characterization of Si during lithiation and delithiation. Indeed, they are often designed to already have Si in an amorphous state and to suppress the formation of crystalline $Li_{15}Si_4$ during cycling. Figure 1 shows SEM images, XRD spectra, and PSDs of the Si used in the electrodes. The SEM images (a, b) show very large Si particles with crystalline features. The XRD spectra (c) show the slurry preparation has not changed the crystallinity of the particles. The Si particles remain highly crystalline with XRD peak widths at the instrumental broadening error (i.e. corresponding to grain sizes greater than 80 nm). Finally, Fig. 1d shows the slurry preparation has reduced the D50 particle size from 34 μm to 21 μm. All these observations indicate the results in this paper are representative of minimally processed highly crystalline Si. Oxides on the order of nanometers are expected from air handling and water processing but should not significantly impact the composition given the size of the Si particles.

Figure 2 shows the voltage capacity plots of the cell described below. In all cells, FEC was added to the base EC:EMC electrolyte to help Si cycling. Indeed, it is well known that a base electrolyte without a solvent or additive to minimize electrolyte reactivity (e.g. FEC, VC) will quickly lead to Si failure. The cell shown in Fig. 2 had 0.92 mg of Si in the electrode and a C-rate corresponding to 2.02 mA. Figure 2a shows the initial lithiation is a long flat plateau, corresponding to the amorphization of crystalline Si.[2,28] The first lithiation capacity is approximately 3000 mAh g^{-1}, short of the theoretical 3579 mAh g^{-1} corresponding to $Li_{15}Si_4$ but high enough to give confidence that the majority of the Si has been lithiated. The delithiation shows a plateau near 0.43 V corresponding to the two-phase delithiation of $Li_{15}Si_4$ into amorphous Li_xSi. The electrochemically active Si therefore does indeed reach full lithiation. The next lithiation shows the expected single phase lithiation of amorphous Si. Significant capacity loss is seen from cycle to cycle. This is expected for this type of electrode as it is metallurgical Si with no graphite and minimal conductive diluent and binder. The advantage of such an electrode is that the thermal signal can be attributed to the behavior of Si alone.

Following the initial lithiation and delithiation at C/20, the cell was cycled in three distinct voltage ranges with different lower voltage cutoffs (170 mV, 70 mV, 5 mV) at four different currents (C/20, C/10, C/7.5, C/5). An upper cutoff voltage of 0.9 V was used for all cycles. For all cycles, a constant voltage step to C/40 followed by a 1 h rest is used at the end of both lithiation and delithiation.

Figure 3 shows the differential capacity curve (dQ/dV) of the second lithiation and where the chosen lower voltage cutoffs are located with respect to the lithiation curve. The lower voltage cutoffs were chosen to correspond to the midpoints in the peaks of the

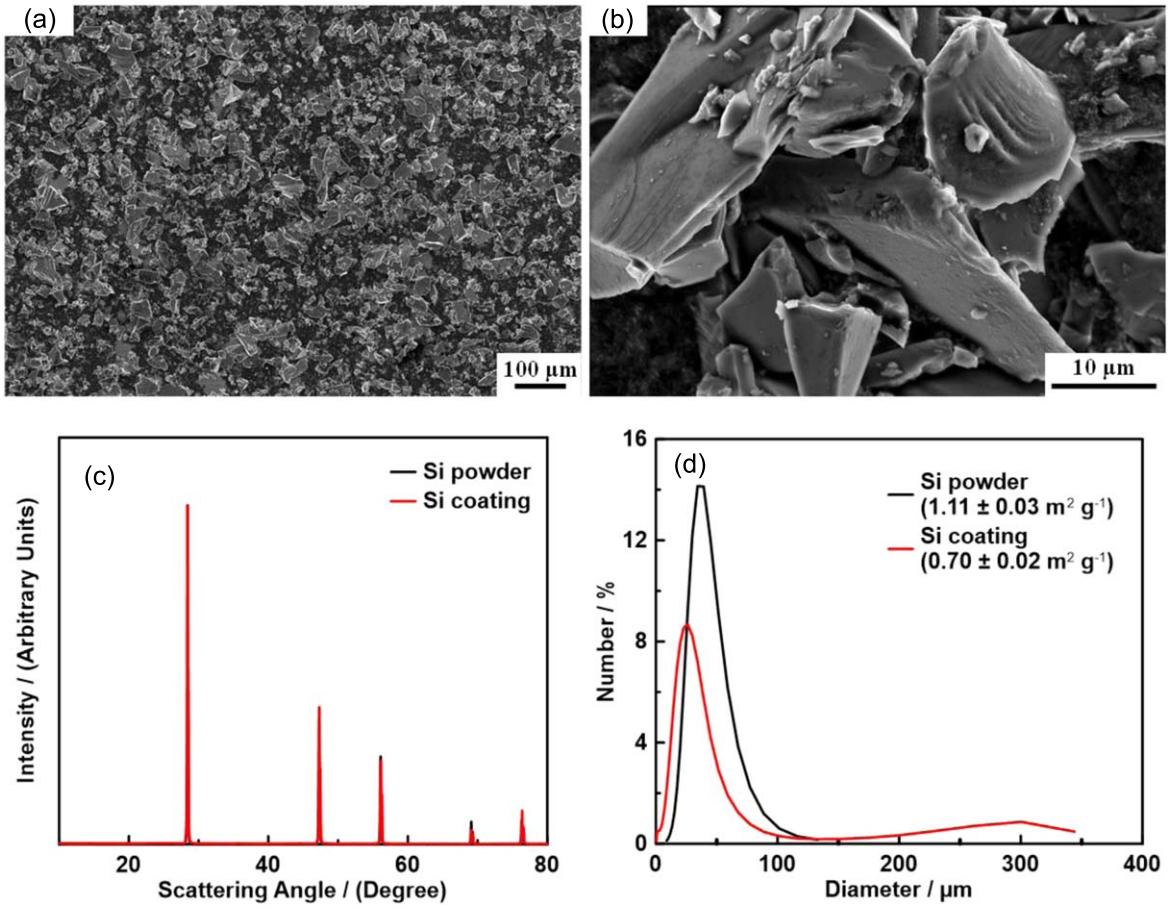

Figure 1. (a)–(b) SEM images of Si electrode. (c) XRD patterns of original Si powder and Si from an electrode coating. (d) PSD and SSA results for Si powder and Si from an electrode coating.

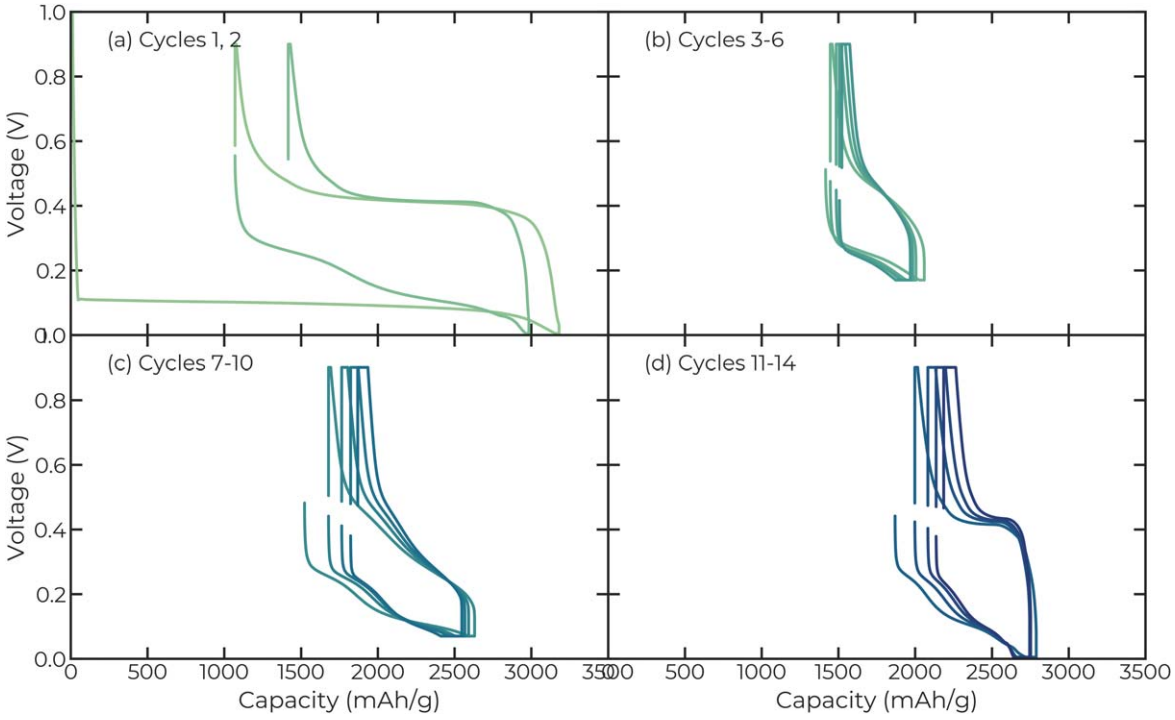

Figure 2. Cycling of a crystalline Si half cell in various voltage ranges. In all cases the upper cutoff voltage was 0.9 V, and a constant voltage segment to C/40 was applied at the end of lithiation and delithiation. (a) Initial cycling to 5 mV at C/20. (b) Cycling to 170 mV (c) cycling to 70 mV and (d) cycling to 5 mV.

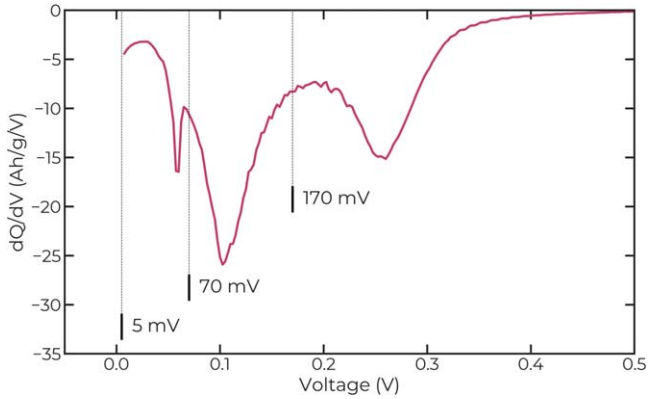

Figure 3. Lower voltage cutoffs chosen for the cycling and their relation to the lithiation differential capacity curves.

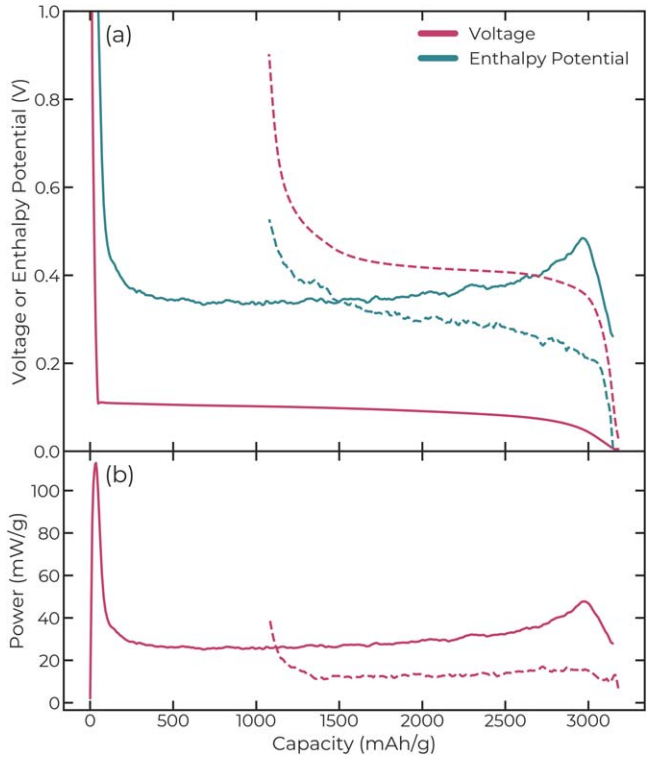

Figure 4. (a) Voltage and enthalpy potential and (b) thermal power of the first lithiation and delithiation of crystalline Si at a C/20. (solid curves lithiation; dashed curves delithiation).

lithiation dQ/dV. These ranges will be discussed in detail in the following sections.

First lithiation: conversion of crystalline Si.—Figure 4 shows the voltage and enthalpy potentials of the first lithiation and delithiation along with the raw thermal power. The general features of the thermal power during the first lithiation of crystalline Si are in good agreement with previous isothermal calorimetry measurements with nano-Si.[14,15] These include an initial exothermic nucleation event and a relatively flat plateau. A notable difference is a rise followed by a decrease in thermal power at the end of lithiation which is not found in Refs. 14, 15. The delithiation voltage profile in Fig. 4a shows the characteristic $Li_{15}Si_4$ plateau, whereas the delithiation voltage profile in Refs. 14, 15 shows a sloping voltage curve indicative of amorphous Li_xSi and absence of $Li_{15}Si_4$. The rise and fall of the thermal power at the end of lithiation in Fig. 4b is therefore attributed to the formation $Li_{15}Si_4$.

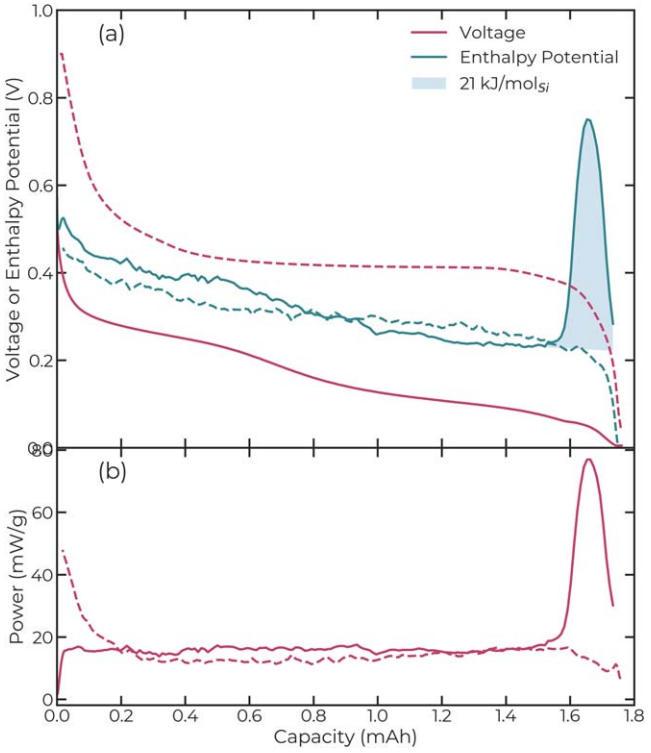

Figure 5. (a) Voltage and enthalpy potential and (b) thermal power of the second lithiation and delithiation of crystalline Si at a C/20 rate. The delithiation has been scaled to match the lithiation to facilitate comparison. (solid curves lithiation; dashed curves delithiation).

The enthalpy potential during initial lithiation is quite high showing there is a tremendous entropy contribution to the initial lithiation, since the impedance related overpotential is known to be small for this rate (comparable to the overpotential obtained at C/1000 in Ref. 6). This is expected as the Si is known to be converted from a highly ordered crystalline state to a disordered amorphous Li–Si phase, in addition, significant heat is expected from the formation of the initial solid electrolyte interphase (SEI). The total lithiation heat is 910 mWh g^{-1}, less than the equivalent measured in Ref. 14 (1509 mWh g^{-1}), however the lithiation rate in the current study was also lower (110 mA g^{-1} vs 188 mA g^{-1} respectively) and the lithiation heats can therefore be considered comparable. The lost electrical work, or entropy production, for the first cycle is 1170 mWh g^{-1}, approximately 20% higher than for the second cycle (970 mWh g^{-1}).

Lithiation to 5 mV: $Li_{15}Si_4$ crystallization.—Figure 5 shows the (a) voltage, enthalpy potential and (b) power during the second cycle. In-situ XRD studies have shown that the Si starts off as a-Si and remains amorphous throughout lithiation until approximately 50 mV where the $Li_{15}Si_4$ phase suddenly crystallizes. This crystallization has been compared to the sudden crystallization of supercooled water.[29] A large exothermic event is clearly visible in the calorimetry data precisely when the crystallization of $Li_{15}Si_4$ is expected to occur. Calculation of an enthalpy of crystallization requires integration of the enthalpy potential peak and an estimation of the amount of $Li_{15}Si_4$ formed. The peak area is estimated by fitting a gaussian with a constant offset. The amount of $Li_{15}Si_4$ formed is estimated by integrating the capacity between 0.40 V and 0.45 V, which is a voltage range centered on the $Li_{15}Si_4$ delithiation plateau and sufficiently broad to account for the overpotentials from the different C-rates.[30] The number of moles of Si taking part in the reaction can then be calculated as $c/F/3.75$, where c is the capacity in the voltage range and F is Faraday's constant. The enthalpy of crystallization for the $Li_{15}Si_4$ can be calculated to be 21 kJ mol_{Si}^{-1}. This dramatic event in the calorimetry data is barely noticeable in

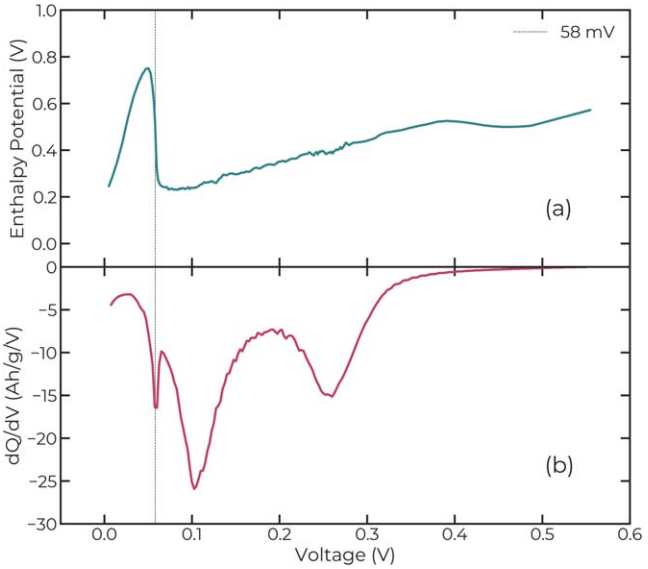

Figure 6. (a) Enthalpy potential and (b) differential capacity of the second lithiation of metallurgical Si at a C/20 rate.

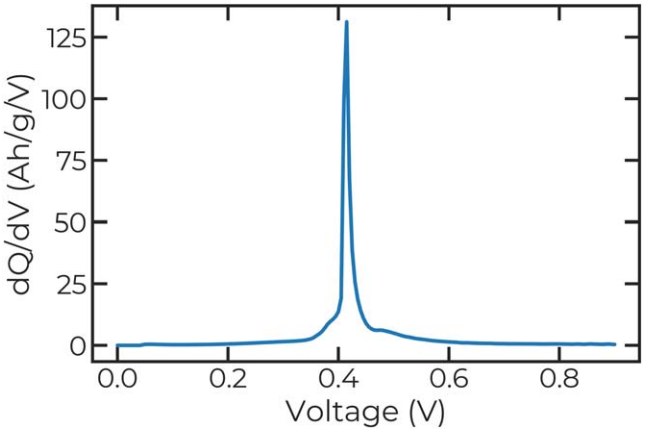

Figure 7. dQ/dV of the delithiation shown in Fig. 5, showing an exceptionally clean two-phase reaction. The voltage was interpolated on a 2.5 mV grid.

the voltage curve. Figure 6 shows (a) the enthalpy potential and (b) dQ/dV as a function of voltage. A small peak near 50 mV in the lithiation dQ/dV has been previously shown to indicate $Li_{15}Si_4$ crystallization. Here, the agreement is perfect and the exothermic event corresponds precisely to the $Li_{15}Si_4$ dQ/dV peak (at 58 mV). The $Li_{15}Si_4$ dQ/dV peak is considerably sharper than normally depicted in the literature. This is likely due to the combination of a slow rate (C/20), exceptional thermal stability, high precision coulometry, and large (initially crystalline) Si particles. A very clean formation of $Li_{15}Si_4$ is supported by the delithiation voltage profile. Figure 7 shows the dQ/dV of the delithiation gives a particularly sharp peak indicative of a clean two-phase $Li_{15}Si_4$ delithiation reaction. Interestingly, Fig. 8 also shows that lithiation continues slightly beyond $Li_{15}Si_4$ crystallization to the 5 mV cutoff. The structural state of the Li–Si phase(s) corresponding to this capacity is not known to the authors.

Figure 6a shows the exothermic peak starting with the $Li_{15}Si_4$ formation but also extending through the end of lithiation. Another cell (0.881 mg Si) was gradually lithiated over the course of 8 cycles, it was subsequently lithiated to 5 mV at C/10. An enthalpy of crystallization of 19 kJ mol_{Si}^{-1} was obtained using the approach described above, in good agreement with the previous result. In

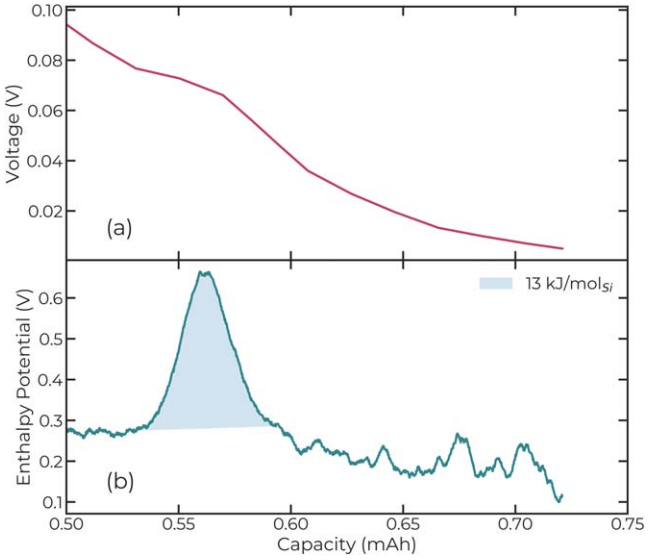

Figure 8. (a) Voltage and (b) enthalpy potential for a cell lithiated at C/100 showing the $Li_{15}Si_4$ crystallization exotherm.

order to determine if the extension of the crystallization peak was purely a kinetic effect, in the following cycle the cell was lithiated at C/10 to 70 mV and then at C/100 to 0 V. Figure 8 shows the voltage (a) and enthalpy potential (b) of this lithiation, which confirms that the crystallization event is limited to the small plateau-like feature in the voltage curve. Application of the same methodology yielded an enthalpy of crystallization of 13 kJ mol_{Si}^{-1}.

The cause for the difference in enthalpy of crystallization between the subsequent cycles is not known. However, the $Li_{15}Si_4$ phase is known to be highly reactive and side reactions occurring at such a slow rate may be affecting the outcome of the measurement.[31] A further refinement of the $Li_{15}Si_4$ phase crystallization enthalpy is given below.

Cycling 170 mV to 0.9 V.—Figure 2b shows cycling of initially crystalline Si in the 170 mV to 0.9 V range. This range is known to be highly reversible, even for macroscopic crystalline Si.[28] Mössbauer spectroscopy[5] and first principles modeling[6,7] have shown this "sloping plateau" (higher voltage peak in Fig. 3) to correspond to the lithiation of mixed Li–Si environments, i.e. from pure Si to a mixture of Li and Si where some Si–Si neighbors remain.

Figure 9a shows the voltage and enthalpy potential capacity plots of the cell cycled over a range of currents. For a given current, the lithiation thermal power, shown in Fig. 9b, is fairly constant indicating a constant entropy contribution. The enthalpy potential is seen to be largely current independent, as expected, and overlaps on lithiation and delithiation showing the reversible nature of the cycling. The divergence at low Li content is likely due to the relaxation of concentration gradients. The kinetic limitations of Si at complete delithiation are well-known.[32]

Figure 10 shows the lost electrical work (voltage hysteresis) and the waste heat (calorimeter) over a cycle are in a good agreement and furthermore extrapolate to significant heat production at zero current showing the current independent nature of the voltage hysteresis in an alloying electrode.

Cycling to 70 mV to 0.9 V.—Figure 2c shows cycling in the 70 mV to 0.9 V range. This range allows cycling of nearly all the Si capacity but keeps the Si amorphous. It yields a voltage curve very similar to those of highly engineered Si materials such as active/inactive Si materials (SiO_x, Si alloys). This range shows two plateau-like features during lithiation. While the first plateau-like feature has been discussed in the previous section. The second plateau-like feature occurs due to the evolution of Li–Si environments with Si–Si

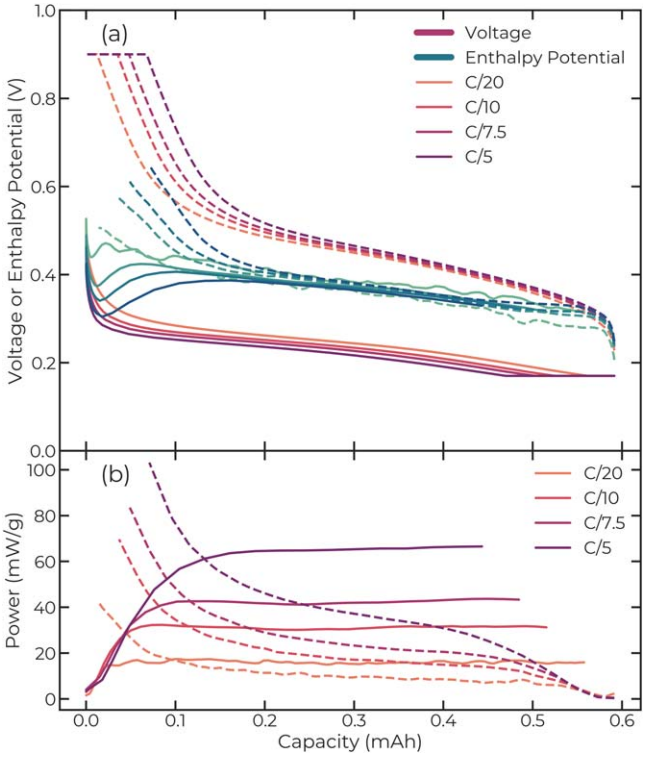

Figure 9. (a) Voltage, enthalpy potential, and (b) thermal power of pure Si cycled in the 170 mV to 0.9 V range at various currents. (solid curves lithiation; dashed curves delithiation). C rates apply to both voltage and enthalpy curves.

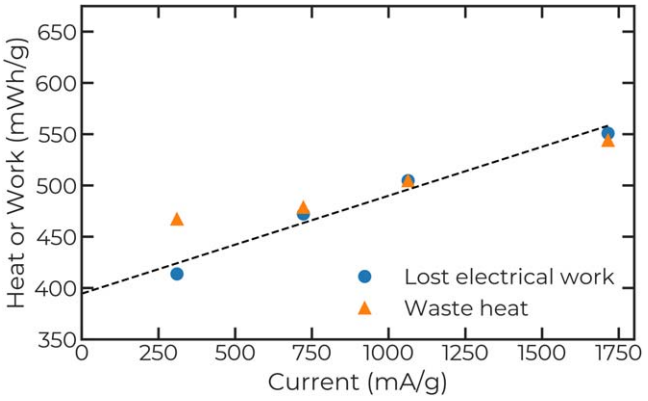

Figure 10. Net heat (calorimetry) and work (voltage hysteresis) of Si in the 170 mV to 0.9 V voltage range.

bonds to predominantly Li–Li environments with only isolated Si atoms.[5,6]

Figure 11a shows the voltage and enthalpy potential capacity plots of the cell cycled over a range of currents. Once again there is good agreement between the enthalpy potential during lithiation and delithiation, Fig. 11b shows the power scales with current and varies nearly monotonically.

Since this is a reversible process, one can therefore take the average of the voltages as the equilibrium potential, which is also shown in Figure 11a. Equation 3 states that the entropy contribution should be the difference between the equilibrium potential and the enthalpy potential. The sloping voltage of amorphous Si lithiation suggests a single phase lithiation reaction with the formation of a Li–Si solid solution. The entropy of mixing for an ideal solid solution is

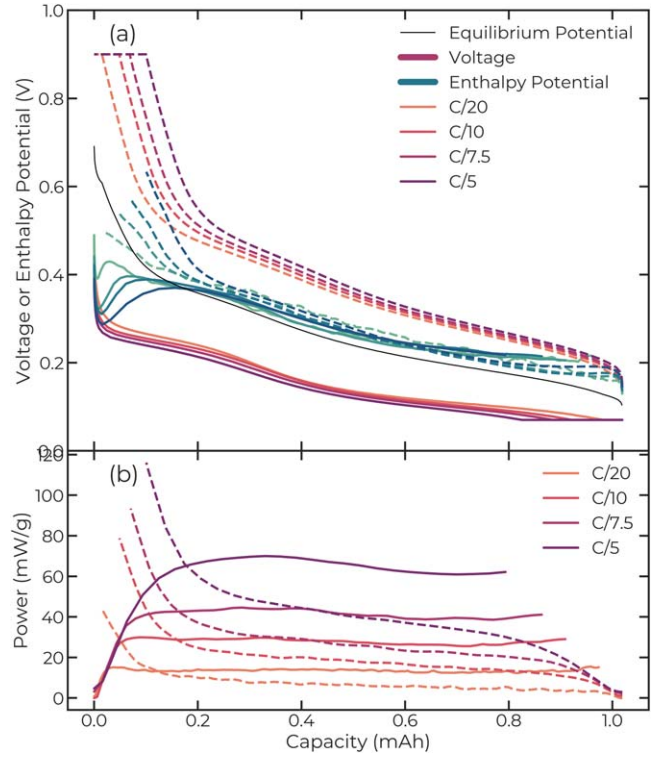

Figure 11. (a) Voltage, enthalpy potential and (b) thermal power for Si between 70 mV and 0.9 V at various currents. (solid curves lithiation; dashed curves delithiation). C rates apply to both voltage and enthalpy curves.

$$\Delta S \propto -(a \ln a + b \ln b) \quad [6]$$

where a and b are mole fractions ($a + b = 1$). In the case of lithiation, the stoichiometry is not expressed as Li_aSi_b but as Li_xSi, performing the substitution $a = \frac{x}{x+1}$, $b = \frac{1}{x+1}$ and taking the derivative with respect to x one obtains

$$\frac{dS}{dx} \propto -\frac{\ln x}{(x+1)^2} \quad [7]$$

Figure 12a shows the difference between the equilibrium potential and enthalpy potential at C/20 of Fig. 11. Figure 12b shows the expected entropy contribution of a solid solution lithiation. There is good qualitative agreement, confirming Eqs. 3 and 7. Indeed the equilibrium potential is initially above the enthalpy potential, crosses after approximately 1/5 of the capacity and remains below the enthalpy potential for the remainder of the lithiation. To a first order, simple entropy of solid solution mixing is therefore sufficient to explain the overall behavior of Si lithiation in the amorphous region.

Figure 13 shows the lost electrical work (voltage hysteresis) and the waste heat (calorimeter) over a cycle are in a good agreement. Comparison to Fig. 10 shows the net heat and work are roughly twice those obtained with a 170 mV, in agreement with their capacity ratios.

Parasitics of reversible Si cycling.—In calculating the heat for Fig. 13, a constant power was subtracted from the calorimeter signal to account for the parasitics. This assumption is based on the premise that parasitic power is constant on the scale of hours and not dependent on whether the cell is cycling.[18] While this assumption holds well for intercalation materials where parasitics seem to follow a $t^{1/2}$ dependence,[33] this may not hold true for materials with large structure and volume changes such as Si. Indeed, experience shows that the consumption of electrolytes in Si containing cells has a time and cycle dependence.[34]

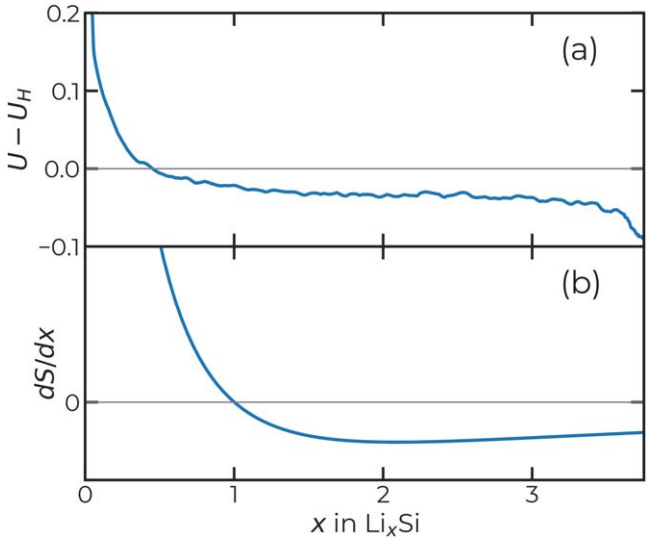

Figure 12. Schematic mixing entropy variation as a function of Li content.

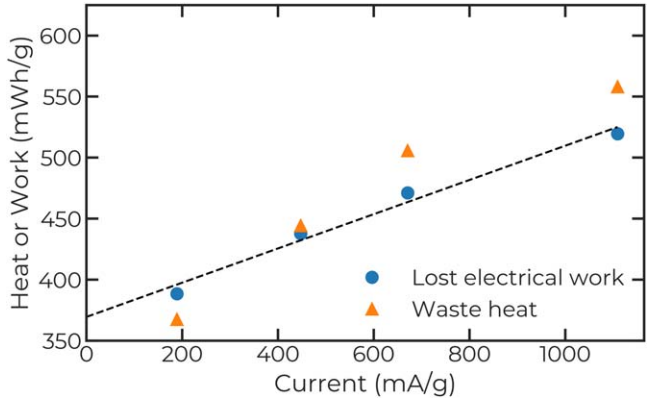

Figure 13. Heat (calorimetry) and work (voltage hysteresis) of Si in the 70 mV to 0.9 V voltage range.

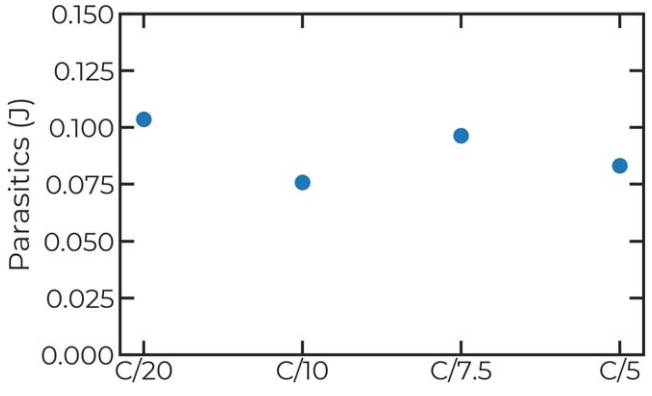

Figure 14. Absolute parasitics obtained over a full cycle when cycling metallurgical Si with a 70 mV lower voltage cutoff.

The results presented in this section were calculated using the raw calorimeter signal. A constant power was *not subtracted* to account for parasitics. The parasitics for a complete cycle can be calculated by subtracting the electrical work (voltage hysteresis) from the waste heat (calorimeter).[12] Figure 14 shows the parasitics for 4 cycles completed at different currents (C/20, C/10, C/7.5, C/5) is nearly identical. If the parasitic power was constant, the parasitic energy for a C/20 cycle would be 4 times higher than a C/5 cycle. The parasitic power

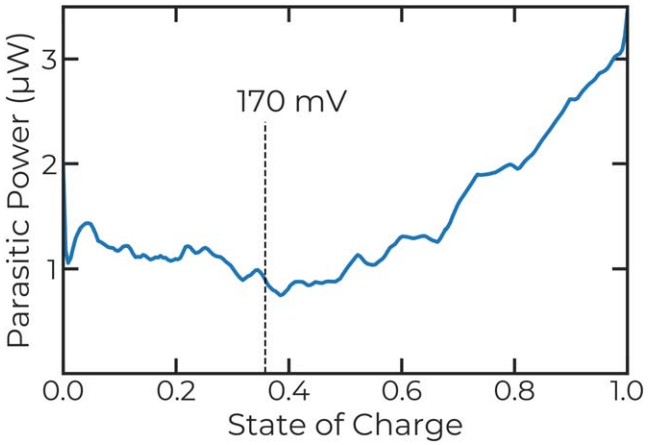

Figure 15. Absolute parasitic power obtained as a function of state of charge (1.0 being fully lithiated).

therefore has some current dependence. Though further studies would be required to extract a functional form, Ref. 34 which discusses the functional form of electrolyte consumption with a cycle and time dependent contributions, would likely be a good starting point. As discussed above, the lithiation and delithiation are following a reversible path in this voltage range. Since the path is reversible, the parasitic power as a function of voltage can be estimated using Eq. 8

$$\dot{q}_p = \bar{\dot{q}} - I\frac{\Delta V}{2} \quad [8]$$

since the entropic terms cancel out for a reversible process and equilibrium potential can be assumed to lie at the midpoint of the voltage hysteresis.[21] Figure 15 shows the parasitics as a function of state of charge (where 1 is the fully lithiated state). This measurement was performed with a cell with 0.881 mg Si, cycled at a constant current of 24 μA between 70 mV and 0.9 V. The lithiation capacity was 0.45 mAh as the cell had already lost some capacity. The parasitic power is initially low at low lithiation levels, after an inflexion point near 0.4, the parasitic power increases monotonically. The state of charge corresponding to a 170 mV cutoff on lithiation is indicated. Cycling Si above 170 mV therefore limits cycling to the region where the parasitic power is lowest. This is in excellent agreement with the body of literature showing much better capacity retention is obtained when cycling Si above 170 mV[28] or operating in a limited capacity range[35] or that $Li_{15}Si_4$ is highly reactive.[31] It is also in good qualitative agreement with Ref. 14 (Fig. 7c) where the parasitics of Si lithiation were calculated using isothermal calorimetry combined with coulometry. Whereas the above analysis assumes the cancelling of reversible entropic terms, the entropic contribution in Ref. 14 was calculated by studying the change in voltage with temperature.

Cycling to 5 mV to 0.9 V.—Figure 2d shows cycling in the 5 mV to 0.9 V range. This range covers the full Si capacity and is known to cause the crystallization of $Li_{15}Si_4$. The enthalpy of crystallization was discussed above, and here the enthalpy potential is considered. Figure 16a shows the voltage and enthalpy potential capacity plots of the cell cycled over a range of currents and (b) the corresponding power measured in the calorimeter. This time there is *no* agreement between the lithiation and delithiation enthalpy potentials, although they are respectively current independent. The distinct enthalpy potential paths are an unambiguous confirmation of the distinct paths in energy space taken by Si during lithiation and delithiation when $Li_{15}Si_4$ crystallization occurs. Figure 17 shows a schematic representation of the free energy (the equilibrium potential is related to the derivative: $U = -\frac{1}{nF}\frac{dG}{dx}$). Figure 17a shows the path taken in a reversible regime as demonstrated in the previous sections with the 170 mV and 70 mV lower voltage cutoffs. Figure 17b shows the

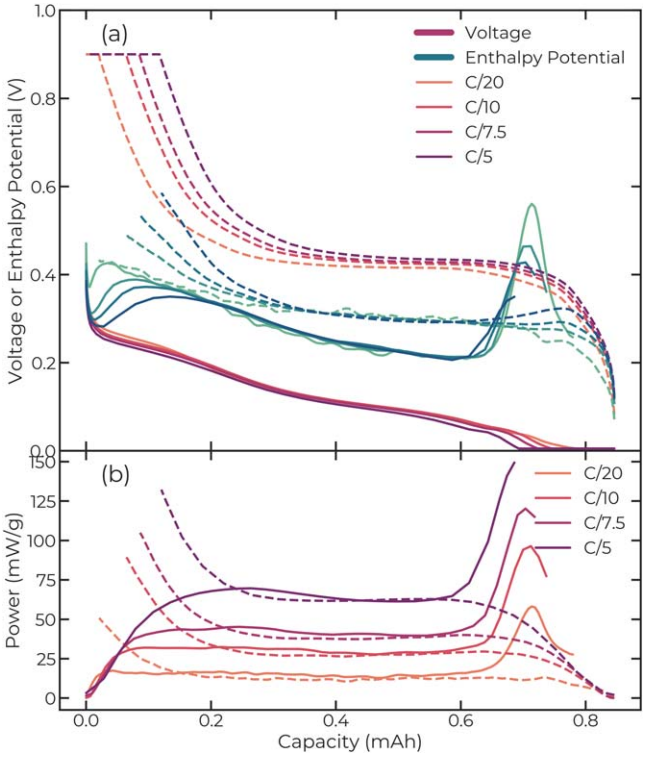

Figure 16. (a) Voltage, enthalpy potential and (b) thermal power for Si cycled between 5 mV and 0.9 V at various currents. (solid curves lithiation; dashed curves delithiation). C rates apply to both voltage and enthalpy curves.

non-reversible path taken when $Li_{15}S_4$ crystallization occurs. The lithiation follows a single phase path (sloping voltage) to x = 3.75, then $Li_{15}Si_4$ crystallizes and the heat released is measured by the calorimeter, finally the delithiation follows a straight two-phase path leading to a voltage plateau. The enthalpy potential is a state variable, its integral over a closed path (cycle) should therefore be zero:

$$\oint_{cycle} U_H dx = 0 \qquad [9]$$

In the previous cases with the lower cutoffs of 170 mV and 70 mV, the enthalpy potential was identical on lithiation and delithiation, showing Eq. 9 to be trivially true. In the case of $Li_{15}Si_4$ crystallization the paths are distinct and the enthalpy potential is much greater on delithiation for the majority of the cycle, with the exception of the moment of crystallization. Numerical integration of the enthalpy potential shows Eq. 9 to hold to within at most a 3% error. The higher enthalpy potential found during most of the delithiation is therefore exactly compensated by the heat released during crystallization, a conclusion that can only be reached with the help of the calorimetry data. Figure 16b shows the power scales with the current even for the crystallization event showing the crystallization to be current driven, and the corresponding enthalpy potential shows that the peak becomes shorter as it becomes wider. The power is not shown for the voltage hold portion as the decreasing current leads to a combination heat of mixing and crystallization. The methodology described above was used to estimate the enthalpy of crystallization for the C/20, C/10, C/7.5, and C/5 cycles. When fitting the gaussian to the peak in the enthalpy potential, the full area of the gaussian was used to estimate the enthalpy of crystallization. Enthalpies of crystallization of 22, 23, 23, 21 kJ mol_{Si}^{-1} were obtained respectively, all in agreement with the results obtained above. Considering all the measured enthalpies of crystallization, the enthalpy of crystallization is estimated to be 21 kJ mol_{Si}^{-1} in the C/5 to C/20 current ranges.

To the authors' knowledge, this is the first report of the enthalpy of crystallization of a-$Li_{15}Si_4$ → x-$Li_{15}Si_4$. The crystallization enthalpy is not negligible compared to the overall heat signal of the cell. Equation 5 shows the enthalpy potential can be useful to evaluate the heat production of a cell. A full cell that undergoes Si crystallization in the field will therefore have significant heat production, which may be of importance to the application.

Previous density functional theory (DFT) calculations have shown that the difference in internal energy (0 K) of the disordered a-$Li_{15}Si_4$ (−0.85 eV/Si) and the more stable crystalline x-$Li_{15}Si_4$ (−1.1 eV/Si) is 25 kJ mol_{Si}^{-1}.[6,7] This is excellent agreement with experiment and may be fortuitous. Indeed reaction enthalpy errors for DFT calculations are expected to be on the order of 5 kJ mol^{-1} [36] and furthermore, DFT phonon calculations have shown that

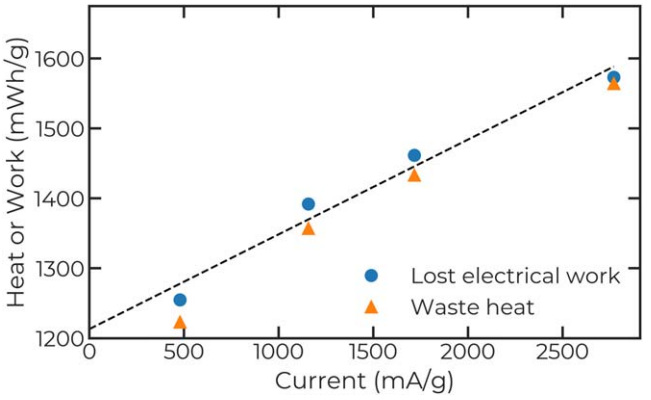

Figure 18. Heat (calorimetry) and work (voltage hysteresis) of Si in the 5 mV to 0.9 V voltage range.

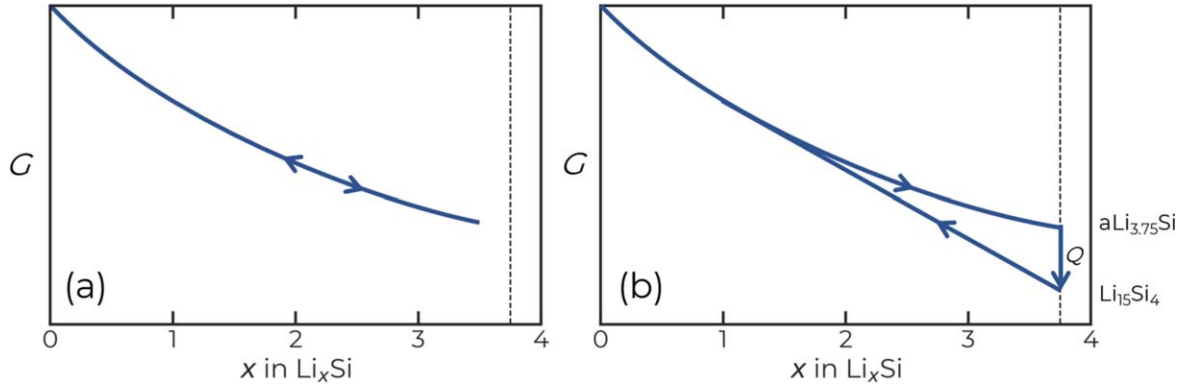

Figure 17. Schematic representation of the path dependence of Si lithiation and delithiation in free energy space. (a) Reversible path, Li_xSi remains amorphous during lithiation and delithiation. (b) $Li_{15}Si_4$ crystallization leading to distinct paths on lithiation and delithiation.

vibration entropic contributions can account for differences of as much as 0.03 eV atom^{-1} (or approximately 15 kJ mol$_{Si}^{-1}$) between Li–Si phases at 40 °C (see Fig. 12 Ref. 37). Nevertheless, first principles calculations are in agreement with the experimentally measured enthalpies of crystallization.

Figure 18 shows the lost electrical work and waste heat, once more showing good agreement. Comparison of Figs. 13 and 18 shows that the waste heat is ∼65% higher in the case of a 5 mV cutoff for only ∼33% more capacity on average. The higher waste heat of Si undergoing crystallization is another possible reason for the need to manage the microstructure of Si, even beyond reasons of capacity retention.

Conclusions

The structural evolution of Si during lithiation and delithiation is uniquely dependent on the cycling conditions and can show either reversible or path dependent behavior. In this paper, metallurgical Si (large crystalline particles of pure Si) is cycled to exhibit both reversible and path dependent cycling while in-operando calorimetry is performed with a high precision isothermal calorimeter. The enthalpy potential and waste heat are studied in both the reversible and path dependent regimes. The enthalpy of crystallization of $Li_{15}Si_4$ is quantified to be 21 kJ mol$_{Si}^{-1}$. The parasitics of pure Si are studied, showing a stronger current than time dependence. The voltage dependence of the parasitic power is quantified, showing increasing parasitics below 170 mV. The results of this paper provide an in-depth study of the calorimetry of metallurgical Si and provide valuable insights into the heat production and energy efficiency of Si as a negative electrode material in Li-ion batteries.

Acknowledgments

Z. Yan would like to thank Michel B. Johnson for his assistance in collecting PSD and SSA data. V. L. Chevrier would like to thank Felix Hanke (Dassault Systèmes) for helpful discussions. Z. Yan and M. N. Obrovac acknowledge funding support from NSERC and Novonix under the auspices of the Industrial Research Chair Program.

ORCID

V. L. Chevrier https://orcid.org/0000-0002-8725-0787
Zilai Yan https://orcid.org/0000-0002-1615-4157
M. N. Obrovac https://orcid.org/0000-0001-5509-3185

References

1. M. N. Obrovac and V. L. Chevrier, *Chem. Rev.*, **114**, 11444 (2014).
2. P. Limthongkul, Y.-I. Jang, N. J. Dudney, and Y.-M. Chiang, *Acta Mater.*, **51**, 1103 (2003).
3. M. N. Obrovac and L. Christensen, *Electrochem. Solid-State Lett.*, **7**, A93 (2004).
4. J. Li and J. R. Dahn, *J. Electrochem. Soc.*, **154**, A156 (2007).
5. J. Li et al., *J. Electrochem. Soc.*, **156**, A283 (2009).
6. V. L. Chevrier and J. R. Dahn, *J. Electrochem. Soc.*, **157**, A392 (2010).
7. V. L. Chevrier and J. R. Dahn, *J. Electrochem. Soc.*, **156**, A454 (2009).
8. G. Assat, S. L. Glazier, C. Delacourt, and J. M. Tarascon, *Nat. Energy*, **4**, 647 (2019).
9. M. M. Huie et al., *J. Phys. Chem. C*, **122**, 10316 (2018).
10. M. M. Huie et al., *ACS Appl. Mater. Interfaces*, **11**, 7074 (2019).
11. D. Chalise, W. Lu, V. Srinivasan, and R. Prasher, *J. Electrochem. Soc.*, **167**, 090560 (2020).
12. L. J. Krause, L. D. Jensen, and J. R. Dahn, *J. Electrochem. Soc.*, **159**, A937 (2012).
13. V. L. Chevrier et al., *J. Electrochem. Soc.*, **161**, A783 (2014).
14. L. M. Housel et al., *ACS Appl. Mater. Interfaces*, **11**, 37567 (2019).
15. W. Li, M. N. Vila, E. S. Takeuchi, K. J. Takeuchi, and A. C. Marschilok, *MRS Adv.*, **5**, 2525 (2020).
16. L. E. Downie, K. J. Nelson, R. Petibon, V. L. Chevrier, and J. R. Dahn, *ECS Electrochem. Lett.*, **2**, A106 (2013).
17. L. E. Downie and J. R. Dahn, *J. Electrochem. Soc.*, **161**, A1782 (2014).
18. L. E. Downie, S. R. Hyatt, A. T. B. Wright, and J. R. Dahn, *J. Phys. Chem. C*, **118**, 29533 (2014).
19. L. E. Downie, S. R. Hyatt, and J. R. Dahn, *J. Electrochem. Soc.*, **163**, A35 (2016).
20. D. S. Hall, S. L. Glazier, and J. R. Dahn, *Phys. Chem. Chem. Phys.*, **18**, 11383 (2016).
21. L. J. Krause, L. D. Jensen, and V. L. Chevrier, *J. Electrochem. Soc.*, **164**, A889 (2017).
22. L. J. Krause, T. Brandt, V. L. Chevrier, and L. D. Jensen, *J. Electrochem. Soc.*, **164**, A2277 (2017).
23. L. J. Krause, V. L. Chevrier, L. D. Jensen, and T. Brandt, *J. Electrochem. Soc.*, **164**, A2527 (2017).
24. K. E. Thomas and J. Newman, *J. Power Sources*, **119–121**, 844 (2003).
25. K. E. Thomas and J. Newman, *J. Electrochem. Soc.*, **150**, A176 (2003).
26. G. M. Koenig, D. Gupta, and Y. Kim, *J. Electrochem. Soc.*, **167**, 120529 (2020).
27. Z. Yan and M. N. Obrovac, *J. Electrochem. Soc.*, **164**, A2977 (2017).
28. M. N. Obrovac and L. J. Krause, *J. Electrochem. Soc.*, **154**, A103 (2007).
29. Y. Jiang, G. Offer, J. Jiang, M. Marinescu, and H. Wang, *J. Electrochem. Soc.*, **167**, 130533 (2020).
30. Y. Cao, B. Scott, R. A. Dunlap, J. Wang, and M. N. Obrovac, *J. Electrochem. Soc.*, **166**, A21 (2019).
31. B. Key et al., *J. Am. Chem. Soc.*, **131**, 9239 (2009).
32. J. H. Ryu, J. W. Kim, Y.-E. Sung, and S. M. Oh, *Electrochem. Solid-State Lett.*, **7**, A306 (2004).
33. A. J. Smith, J. C. Burns, D. Xiong, and J. R. Dahn, *J. Electrochem. Soc.*, **158**, A1136 (2011).
34. R. Petibon et al., *J. Electrochem. Soc.*, **163**, A1146 (2016).
35. M. Gauthier et al., *Energy Environ. Sci.*, **6**, 2145 (2013).
36. A. Benisek and E. Dachs, *Contrib. to Mineral. Petrol.*, **173**, 90 (2018).
37. V. L. Chevrier, J. W. Zwanziger, and J. R. Dahn, *J. Alloys Compd.*, **496**, 25 (2010).